142 GHz Sub-Terahertz Radio Propagation Measurements and Channel Characterization in Factory Buildings

Shihao Ju, Dipankar Shakya, Hitesh Poddar, Yunchou Xing, Ojas Kanhere, and Theodore S. Rappaport
NYU WIRELESS, Tandon School of Engineering, New York University, Brooklyn, NY, 11201
{shao, dshakya, hiteshp, ychou, ojask, tsr}@nyu.edu

***Abstract*—This paper presents sub-Terahertz (THz) channel characterization and modeling for an indoor industrial scenario based on radio propagation measurements at 142 GHz in four factories. We selected 82 transmitter-receiver (TX-RX) locations in both line-of-sight (LOS) and non-LOS (NLOS) conditions and collected over 75,000 spatial and temporal channel impulse responses. The TX-RX distance ranged from 5 to 87 m. Steerable directional horn antennas were employed at both link ends and were switched between vertical and horizontal polarization. Measurements were conducted with low RX and high RX antenna heights of 0.5 m and 1.5 m to characterize the propagation channel for close-to-floor applications such as automated guided vehicles. Results show that the low RXs experience an average path loss increase of 10.7 dB and 6.0 dB at LOS and NLOS locations, respectively. In addition, channel enhancement measurements were conducted using a steerable large flat metal plate as a passive reflecting surface, demonstrating omnidirectional path loss reduction from 0.5 to 22 dB with a mean of 6.5 dB. This paper presents the first statistical channel characterization and path loss modeling for industrial scenarios at sub-THz frequencies, highlighting the potential for ultra-broadband factory communications in the 6G era.**

***Index Terms*—Terahertz; Radio Propagation; Indoor Factory; Channel Measurement; Channel Modeling; 140 GHz; 5G; 6G; passive reflecting surface (PRS); Reconfigurable intelligent surface (RIS)**

I. Introduction

Smart factories and smart manufacturing play a significant role in Industry 4.0, also known as the Fourth Industrial Revolution, envisioning the interconnection and intelligent collaborative operation of machines, sensors, and robots. Modern factories use cutting-edge technologies, such as augmented reality remote support, computer vision-aided product inspection, and machine learning-based preventive facility maintenance. These applications place high demands on wireless systems, compared to daily scenarios like office and residential environments, due to the increased use of wireless devices and remote operation, which requires ultra-high system throughput and reliability. The use of millimeter-wave (mmWave) and Terahertz (THz) communication, which offer wider bandwidths than conventional wireless systems, has proven promising due to their spectrum availability and millimeter-level wavelengths, enabling ultra-broadband communications and steerable pencil beams generated by large antenna arrays with a massive number of elements [1].

Wireless signals in factories face unique challenges due to the smooth metallic surfaces of machinery and robotics, which are more reflective and less penetrative than common building materials like drywall [11]. Therefore, extensive channel measurements and accurate channel models to establish dedicated wireless systems for manufacturing factories are essential. Pioneering wideband multipath measurements were conducted at 1.3 GHz in five factory buildings for line-of-sight (LOS) and non-LOS (NLOS) propagation [11]. The path loss measurements at 50 locations in [11] reported an omnidirectional path loss exponent (PLE) of 2.15 using the close-in (CI) free space reference distance path loss model with the reference distance equal to ten wavelengths. Schmieder et al. [2] presented 28 GHz channel measurements in a circle-shaped machine hall with a diameter of 63 m. The transmitter (TX) height was 7 m. The receiver (RX) height was 4 m and 1.7 m for LOS and NLOS measurements, respectively. According to Schmieder et al. [2] the omnidirectional PLEs were 1.8 and 2.0 for LOS and NLOS measurements, respectively and the channel has dense multipath components (MPC) with delays up to 1000 ns. Moreover, blockage significantly affects the LOS component but has limited influence on the overall channel gain. Additionally, Ito et al. [6] presented 28 GHz channel measurements having the RX move on linear routes. The LOS and NLOS measurements in [6] showed the PLEs to be 1.8 and 2.8, respectively. Moreover, the root mean square (RMS) delay spread and RMS angular spread of arrival were much larger in the indoor factory (InF) than the indoor office (InH) scenario in both LOS and NLOS [6]. Furthermore, Wang et al. [7] conducted 28 GHz channel measurements in a large factory-like laboratory over 5–25 m separation distance. A peer-to-peer setup was used for two sets of measurements with antenna heights at 0.8 and 1.6 m, producing PLEs of 2.05 and 1.79, respectively. The findings suggest that occlusion caused by surrounding objects leads to a larger PLE and a smaller delay spread when antenna height is lower than nearby

Manuscript received April 17, 2023; first revised August 7, 2023; second revised November 13, 2023; accepted November 15, 2023. This work was supported in part by the NYU WIRELESS Industrial Affiliates Program, in part by NOKIA, in part by the three National Science Foundation (NSF) Research under Grant 1909206, Grant 2037845, and Grant 2216332. (Corresponding author: Shihao Ju.)

The authors are with the NYU WIRELESS Research Center, NYU Tandon School of Engineering, New York University, Brooklyn, NY 11201 USA (e-mail: {shao, dshakya, hiteshp, ychou, ojask, tsr}@nyu.edu).

TABLE I: EXISTING MMWAVE AND SUB-THZ CHANNEL MEASUREMENTS AND MODELING FOR INDOOR FACTORIES COMPARED WITH CHANNEL CHARACTERISTICS IN THIS PAPER AS THE LAST ROW. ASA AND ASD STAND FOR ANGULAR SPREAD OF ARRIVAL AND DEPARTURE, RESPECTIVELY.

Frequency (Bandwidth)	Scenario	Space Dimension (m)	TX-RX Separation Distance	Path Loss Exponent	Mean RMS Delay Spread	Mean RMS ASA	Reference
28 GHz (2 GHz)	Machine hall LOS & NLOS	63 D×18.5 H	11.5–42 m	(CI) LOS: 1.8 NLOS: 2.0	LOS: 54 ns NLOS: 75 ns	LOS: 35° NLOS: 80°	[2]
28 GHz (2 GHz)	Machine workshop LOS & NLOS	40.5 L×15.5 W ×4.6 H	4–26 m	(ABG) LOS: 2.3 NLOS: 3.0	LOS: 23 ns NLOS: 33 ns	LOS: 36° NLOS: 64°	[3]
28 GHz (2 GHz)	Fabrication lab LOS & NLOS	13 m^2	4–10 m	(CI) LOS: 1.3 NLOS: 2.7	19.6 ns	50°	[4]
28 GHz (0 Hz)	Factory Aisle LOS & NLOS	—	5–100 m	(FI) NLOS: 4.1	—	—	[5]
28 GHz (2.4 GHz)	Engineering workshop LOS & NLOS	70 L × 30 W	2–10 m	(FI) LOS: 1.8 NLOS: 2.9	LOS: 40 ns NLOS: 47 ns	LOS: 66° NLOS: 100°	[6]
28 GHz (2.4 GHz)	Large lab LOS & NLOS	33.3 L × 7.7 W × 3 H	2–10 m	(CI) 1.8	13 ns	42°	[7]
30 GHz (6.75 GHz)	Machine hall LOS & NLOS	70 L × 15 W	5–45 m	(CI) LOS: 1.9 NLOS: 3.3	LOS: 41 ns NLOS: 36 ns	(ASD) LOS: 23° NLOS: 28°	[8]
60 GHz (6.75 GHz)	Production hall LOS & NLOS	171 L × 74 W × 16 H	4–30 m	(ABG) LOS: 1.6 NLOS: 1.7	LOS: 29 ns NLOS: 49 ns	(ASD) LOS: 35° NLOS: 38°	[9]
108 GHz (2 GHz)	Manufacturing hall LOS	—	0.5–5 m	(CI) LOS: 1.7	LOS: 4.1 ns	—	[10]
142 GHz (1 GHz)	**Factory halls LOS & NLOS**	**110 L × 30 W × 25 H**	**5–85 m**	**(CI) LOS: 1.8 NLOS: 3.1**	**LOS: 14.0 ns NLOS: 12.8 ns**	**LOS: 33.8° NLOS: 43.7°**	[30], [31], and this paper

metal machines. The modeling results demonstrate that the RMS delay spread is directly proportional to the distance between the TX and RX, and the angular spread also increases with the TX-RX distance. 60 GHz channel measurements in five representative industrial scenarios, such as mechanical room and experimental hall, using commercial off-the-shelf 802.11ad routers, and derived channel statistics and modeling parameters such as the number of clusters, cluster delay, and cluster power were presented in [12]. Around 70 gigabytes of channel measurement data were collected and analyzed to obtain a statistical channel model in [12], and it was concluded that mmWave communication in industrial environments was viable and simpler compared to a typical home or office environment. Finally, Al-Saman et al. [10] conducted vector network analyzer (VNA)-based channel measurements at 108 GHz with 2 GHz sweeping bandwidth in three manufacturing environments over 2–5 m separation distance. All measured locations were in LOS condition, where the PLEs were 1.6–1.9. High K-factor values were observed in [10] at short TX-RX separation distances below 2 m. The RMS delay spread varied between 3 ns to 24 ns. Table I summarizes the existing mmWave and sub-THz channel measurement campaigns and channel characteristics in factories, where the measurement results in this paper are included in the last row.

This work presents a 142 GHz radio propagation measurement campaign in four factory buildings in Brooklyn, NY. Extensive channel measurements using steerable directional horn antennas were conducted at 16 TX locations and 60 RX locations across four factories, resulting in 20 LOS location pairs, 58 NLOS location pairs, and four outage location pairs over a TX-RX separation distance from 5 m to 85 m. Section II details the four factory environments and measurement equipment and procedure used to achieve a complete angular channel profiling from both TX and RX ends. Directional and omnidirectional path loss modeling with polarization effect and comprehensive statistical analysis of temporal and spatial channel parameters for the indoor factory (InF) scenario are presented in Section III. In addition, the extracted factory channel characteristics are compared to the previous measurement results in InH and urban environments. Section IV compares channel characteristics at low (0.5 m) and high RX (1.5 m) antenna heights to investigate the impact of proximity to the floor in heavily cluttered factory environments. Section V demonstrates a signal enhancement approach by deploying a rotatable flat metal plate as a passive reflecting surface (PRS) and shows that the omnidirectional received power increases

from 0.5 dB to 22 dB with a mean of 6.5 dB. Concluding remarks are provided in Section VI.

II. Channel Measurements in Factories

A. Measurement Equipment

The 142 GHz InF channel measurement campaign used a sliding correlation-based wideband channel sounder with a carrier frequency at 142 GHz [13]. The TX baseband unit generated a pseudorandom noise (PN) sequence at a 500 MHz chip rate and mixed it with an intermediate frequency (IF) of 7 GHz. The TX radio frequency (RF) unit upconverted the modulated IF signal to a center frequency of 142 GHz and radiated through a directional and steerable horn antenna. The RX RF unit employed the identical horn antenna and downconverted the received RF signal to the same IF frequency at 7 GHz. The RX baseband unit then demodulated the IF signal to I and Q baseband signals and performed sliding correlation to output a narrowband (62.5 kHz) time-dilated channel impulse response [14]. Twenty consecutive channel impulse responses are squared and averaged, which creates a power delay profile (PDP) that is later sampled by an oscilloscope and recorded by a computer. Such power averaging reduced the thermal noise level and took a total acquisition time of 655 ms.

The identical horn antennas at TX and RX had 27 dBi gain and 8° half power beamwidth (HPBW). The two horn antennas were mounted on software-controlled gimbals and steered in the azimuth and elevation planes with sub-degree accuracy. A 90° waveguide twist switched the horn antennas between vertical and horizontal polarizations for co- and cross-polarized channel characterization. The 142 GHz channel sounder had a null-to-null RF bandwidth of 1 GHz and can measure the propagation path loss up to 152 dB [13]. Two separate, low-phase noise Rubidium reference clocks are used at the TX and RX for their short and long-term stability, which are connected by a cable for back-to-back synchronization before the measurements every day. Once the measurement starts, the two clocks are disconnected and start drifting off; the frequency offset manifests as a PDP drift in the time domain. Such a time drift is often tractable and compensated by a synchronization procedure. The synchronization procedure consists of three measurements of frequency drift before, in the middle of, and after routine channel measurements at each TX-RX location. A linear fit between the three drift measurements produced a drift rate that was satisfactory in compensating PDP time drift and aligning directional PDPs measured from unique pointing angles and at the same location.

B. Measurement Environment

The 142 GHz propagation measurements were conducted in four factory buildings in Brooklyn, NY. These factory buildings constitute a wide range of factory sizes, layouts, and manufacturing facilities, which are described in detail as follows:

1) Site A: Factory Building

Factory A (∼104 m L× 39 m W × 25 m H) was partitioned by glass, concrete, and plaster walls into manufacturing labs and conference rooms covered by large glass windows with metal frames, as shown in Fig. 1. A mezzanine floor was built above the rooms along external facades with a height of 3.7 m above the ground, leaving a 7 m wide open corridor at the center of the building. RX12 and RX16 were in an outage from TX6. The TX was set to 3 m above the ground, except that TX4 was set at 3 m high on the mezzanine floor, having a height of 6.7 m above the ground. The RX was set to 1.5 m above the ground. Table II summarizes the measurements conducted in factory A.

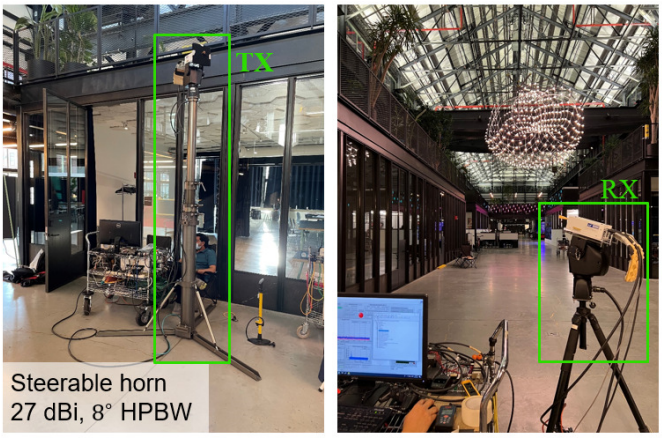

Fig. 1: Measurements in factory A. The TX was set at 3 m, and the TX was set at 1.5 m. The ceiling height of the building is 25 m.

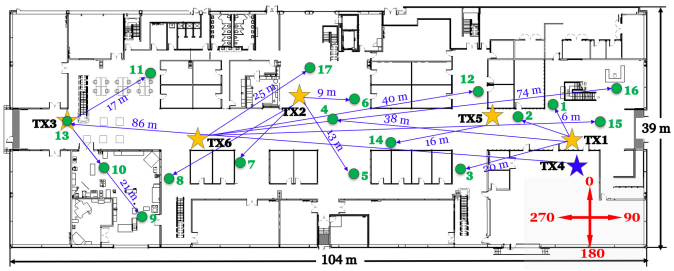

Fig. 2: TX and RX locations in Factory A. Six TX locations are denoted as stars, and 17 RX locations are denoted as circles, resulting in 27 TX-RX location pairs for channel measurements.

2) Site B: Electronics Manufacturing Facility

Factory B is a single-story structure performing a complete production cycle, such as manufacturing, testing, and assembly. We selected three production areas for channel measurements, including automated manufacturing, testing, and assembly. Factory B had heavy clutter containing massive metal objects such as robotics, partitions made of plaster, drywall, machinery, and workstations as shown in Fig. 3. Table II summarizes the measurements conducted in factory B. TXs are often placed close to walls, pillars, and large furniture. However, because of the low ceiling height of 3 m and many large equipment and machinery in factory B, TX1 was placed in the center of the areas as ceiling-mounted access points to alleviate penetration loss and avoid an outage.

3) Site C: Warehouse Facility

Factory C (∼72 m L× 30 m W × 4 m H) was a mid-size concrete building. As shown in Fig. 5, large metal multi-layer

This article has been accepted for publication in IEEE Transactions on Wireless Communications. This is the author's version which has not been fully edited and content may change prior to final publication. Citation information: DOI 10.1109/TWC.2023.3337601

TABLE II: Number of LOS and NLOS measurements conducted at 142 GHz in four different factory environments for a fixed TX height of 2.5 m and high and low RX heights (1.5 m and 0.5 m) for TX-RX distances ranging from 5.6 – 86.5 m.

Environment	High RX (RX Height = 1.5 m)				Low RX (RX Height = 0.5 m)				PRS Used	Tx-Rx Distance
	Total	LOS	NLOS	Outage	Total	LOS	NLOS	Outage		
Factory A	27	10	15	2	—				No	6.5 m – 86.5 m
Factory B	20	3	17	—	—				No	5.6 m – 31.0 m
Factory C	8	0	6	2	3	3	0	—	No	7.7 m – 37.6 m
Factory D	12	3	9	NA	12	1	11	—	Yes	7 m – 35.1 m
Total	**67**	16	47	4	**15**	4	11	—	—	**5.6 m – 86.5 m**

Fig. 3: Measurements in factory B. The TX was set at 2.5 m, and the RX was set at 1.5 m.

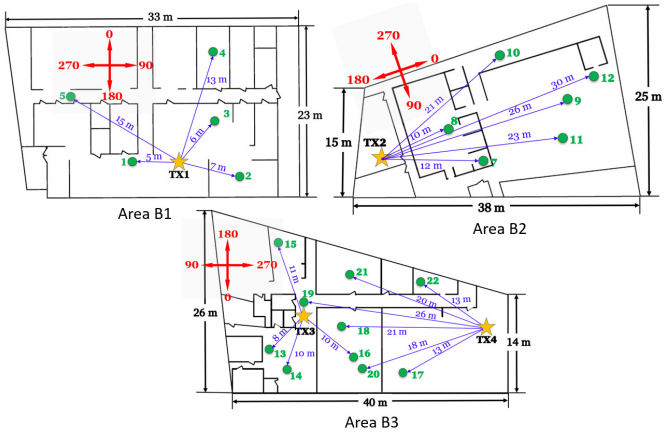

Fig. 4: TX and RX locations in Factory B. Four TX locations are denoted as stars, and 20 RX locations are denoted as circles, resulting in 20 TX-RX location pairs for channel measurements.

shelves with a height of 3 m and a spacing distance of 1.5 m were placed at two sides of the building, creating a 2 m wide walkway in the center. These large metal shelves were filled with cardboard boxes containing metal electronic components, plastic, and paper. Table II summarizes the measurements conducted in factory C.

4) Site D: Manufacturing Space

Factory D (∼35 m L× 25 m W × 5 m H) was a single large room for lightweight manufacturing and production, with various machineries such as laser cutters, CNC machines, and 3D printers. Large glass window panels coated with metallic frames covered the exterior walls on the north, south, and east of this room, whereas thick drywall constituted the wall on the west, as shown in Fig. 7. Plastic tables and wooden chairs were placed in a few office regions. Black-filled circles in Fig. 8 represent concrete pillars that created strong reflections during channel measurements. Table II summarizes the measurements

Fig. 5: Measurements in factory C. The TX was set at 2.5 m, and the RX was set at 1.5 m and 0.5 m.

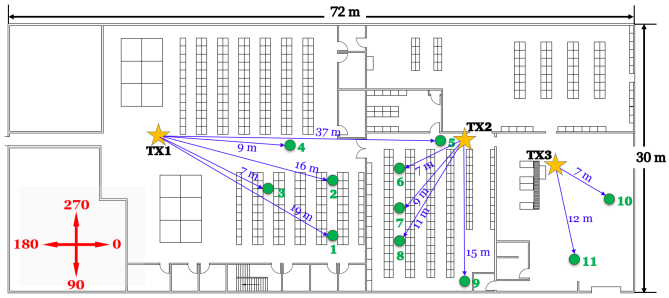

Fig. 6: TX and RX locations in Factory C. Three TX locations are denoted as stars, and 11 RX locations are denoted as circles, resulting in 11 TX-RX location pairs for channel measurements.

conducted in factory D.

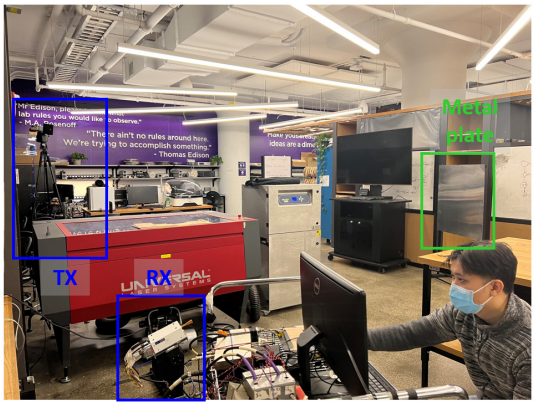

Fig. 7: Measurements in factory D. The TX was set at 2.5 m, and the RX was set at 1.5 m and 0.5 m.

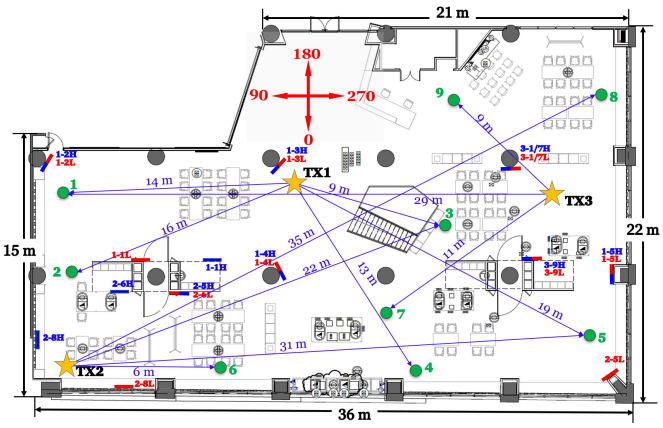

Fig. 8: TX and RX locations in Factory D. Three TX locations are denoted as stars, and nine RX locations are denoted as circles, resulting in 12 TX-RX location pairs for channel measurements. The short blue and red bars denote the PRS positions for high and low RXs, respectively.

C. Measurement Procedure

We propose a new measurement procedure for channel measurements using rotatable directional antennas. This measurement procedure differs from the procedure adopted in our previous indoor and outdoor 142 GHz measurement campaign. The indoor 142 GHz measurements conducted eight TX-RX antenna pointing configurations, where two distinct TX angles were measured with RX omnidirectional sweeps [15], [16]. The outdoor 142 GHz measurements identified potential TX angles which may deliver sufficient power at RX by visual inspection, where the number of measured distinct TX angles depends on the local environment. Most radio propagation measurements conducted at sub-THz frequencies adopted rotatable directional antennas because of easy accessibility and high antenna gain. Most setups placed the TX at one side of the environment and fixed the TX pointing angle while sweeping RX antennas in steps in the azimuth plane [17]–[19]. Fixing the TX antenna at one or a few pointing angles only provides limited TX angular statistics (i.e., AOD characterization) but greatly reduces the overall measurement time (still typically a few hours) for each location, compared to sweeping the TX antenna in steps in the azimuth plane.

The proposed measurement procedure provides a complete view of TX angular statistics by performing a continuous 360° RX scan before RX stepped rotations for PDP measurements. A continuous 360° RX scan takes six seconds, much less than 3 minutes of an RX stepped rotation. For a TX-RX location pair, we first identify the initial TX and RX antenna pointing angles in the azimuth and elevation planes showing the strongest received power, which is often the boresight direction for LOS locations or a strong reflection direction for NLOS locations. The TX antenna is rotated from the initial direction in step increments of the antenna HPBW (8°) in the azimuth plane, resulting in 45 TX directions. We conduct a continuous 360° azimuth scan of the RX antenna and record the peak multipath power for every TX direction. The peak multipath power represents the maximum possible received power along a TX direction regardless of the RX direction. The maximum of the 45 peak multipath powers represents the strongest received power at this TX-RX location pair among all TX and RX angles. Overall, this continuous scan takes five minutes and allows for identifying TX angles that can present sufficient received power at the RX.

We adopt two thresholds to identify valid TX directions, which are 30 dB below the maximum peak multipath power and 10 dB above the average noise floor. The TX directions with peak multipath powers exceeding the minimum of the two thresholds are considered valid. Then, the PDP measurements are only conducted at valid TX directions without compromising the completeness of TX angular statistics. For each valid TX direction, the RX was rotated at step increments of 8° in the azimuth plane. The RX was then uptilted and down tilted by 8° and conducted the exact stepped azimuthal sweep to acquire signal at three elevation angles. Note that the measurement approach using three elevation angles around the boresight captured most of the signal power of the boresight path and reflection paths from vertical obstructions such as walls and pillars [20], but ceiling and ground reflections from large elevation angles might not be detected. One directional PDP was recorded at each RX rotation step. For example, ten valid TX directions correspond to at most 10 (TX azimuth)×45 (RX azimuth)×3 (RX elevation) =1350 directional PDP measurements at this location. The rotation step was set to the antenna HPBW based on the power combining model in [20], which allowed the directional PDPs to be synthesized into a faithful omnidirectional PDP for omnidirectional channel modeling. The directional PDPs from every unique TX-RX pointing angle were synchronized in the time domain and summed together non-coherently in the power domain to reconstruct an omnidirectional PDP for each measured TX-RX location pair.

The measurements for each TX and RX location were conducted for two antenna polarization configurations: V-V and V-H. Once the V-V measurements are completed, identical RX azimuth sweeps are conducted with the V-H antenna polarization. The identical three RX azimuthal sweeps at three elevation planes are performed with the V-H configuration only for those TX pointing angles in which the peak multipath power for the V-V configuration is at least 25 dB above the noise floor because the free space cross-polarization discrimination (XPD) provided by the 90° waveguide twist was measured to be 27.3 dB [21]. The gap of 2.3 dB was left for measurement error tolerance.

III. 142 GHz Channel Characterization for Indoor Factories

This section presents channel characterization and modeling for InF based on extensive radio propagation measurements conducted at 142 GHz in the four factory sites in 2021 and 2022. The measurements provide large-scale path loss and spatial-temporal channel characteristics that are useful for indoor wireless networks in factories for future sub-THz communications. 16 TX locations and 60 RX locations were selected in the 142 GHz measurement campaign. Overall, measurements were conducted at 82 location pairs (i.e., a pair

of TX and RX locations), including 20 LOS location pairs, 58 NLOS location pairs, and four outage location pairs over a wide distance range from 5 m to 85 m, which yielded over 75,000 directional PDPs for channel modeling.

Measurements with co-polarized (V-V) antennas and cross-polarized (V-H) antennas were conducted at each location. Besides four outage locations, 78 locations detected power with co-polarized antenna orientation. However, due to the antenna XPD of 27 dB in free space and the limited dynamic range (i.e., maximum measurable path loss of 152 dB) of the channel sounding system, only 30 locations detected power with cross-polarized antenna orientation consisting of 19 LOS locations and 11 NLOS locations.

A. 142 GHz Path Loss Modeling for Co- and Cross-Polarized Antenna Configurations

We present the well-known CI free space reference distance path model for omnidirectional and directional path loss measurement data because the CI path loss model has been proven to be superior for accurately modeling path loss over many environments and frequencies [22]. A single parameter is used to characterize the distance-dependent average power in the CI path loss model, PLE, denoted as n. $\mathrm{PL}^{\mathrm{CI}}$ represents the path loss in dB scale, which is a function of distance and frequency [15], [22]–[25]:

$$\mathrm{PL}^{\mathrm{CI}}(f,d)[\mathrm{dB}] = \mathrm{FSPL}(f,d_0) + 10n\log_{10}\left(\frac{d}{d_0}\right) + \chi_\sigma^{\mathrm{CI}}, \tag{1}$$

$$\text{for } d \geq d_0, \quad \text{where } d_0 = 1\mathrm{m} \tag{2}$$

where d is the 3-D TX-RX separation distance and d_0 is the reference distance. $\mathrm{FSPL}(f, 1\ \mathrm{m})$ denotes the free space path loss (FSPL) in dB at a reference distance of $d_0 = 1$ m at the carrier frequency f: $\mathrm{FSPL}(f, 1\ \mathrm{m})[\mathrm{dB}] = 20\log_{10}\left(4\pi f \cdot 10^9/c\right) = 32.4[\mathrm{dB}] + 20\log_{10}(f)$. We use d_0 = 1 m as the reference distance, which satisfies the far-field assumption and has been validated through free-space propagation calibration measurements [13]. $\chi_\sigma^{\mathrm{CI}}$ denotes shadow fading (SF), commonly modeled as a normal random variable with zero mean and σ standard deviation in dB. The CI path loss model uses the FSPL at the reference distance as a fixed intercept and finds a straight line fit to the measured path loss data that achieves the minimum mean square error [15], [22]–[25].

For the special case of cross-polarization measurements, the CI path loss model is extended by adding a constant attenuation parameter of XPD, known as the close-in reference distance with XPD (CIX) path loss model. The CIX path loss model uses the co-polarization PLE (n_{co}) derived from the CI model for V-V path loss data that are measured at identical locations and optimizes the XPD factor that best fits the measured cross-polarized path loss data with minimum mean square error. This optimized XPD derived from path loss represents a gross polarization mismatch caused by antennas and multipath channels.

B. Directional path loss models for co- and cross-polarized antennas

Directional path loss models are useful for modeling sub-THz systems that deploy large antenna arrays for beamforming, beam steering, and beam management. As described in Section II-C, the TX and RX horn antennas were rotated in the azimuth and elevation planes to capture signal power from the 3-D space. One directional PDP measurement was conducted at every unique TX and RX antenna pointing angle combination. The received power is calculated by non-coherently integrating a directional PDP in the time domain (i.e., the area under a PDP). TX and RX antenna gains were removed for each received power to create a directional path loss model.

Thus, we consider three types of directional PDPs for directional path loss modeling: LOS, NLOS, and NLOS-Best. For each location in the LOS scenario, only one directional PDP represents the LOS direction that the TX and RX antennas are pointed at each other, aligned on boresight with no obstructions between them. All the other pointing directions except for the LOS direction are defined as NLOS directions, which also includes the case where the TX and RX antennas have a clear LOS path to one another, but the antennas are not aligned on boresight. Furthermore, the NLOS-Best case represents the NLOS direction, resulting in the strongest received power for each TX-RX location pair. The NLOS-Best direction denotes the single strongest measured directional PDP from the NLOS data at each TX-RX location pair. Note that the pointing direction adjacent to the LOS direction may have the strongest received power among all NLOS directions due to the effect of the antenna pattern. However, this LOS-adjacent direction is excluded from the NLOS-Best direction selection because it is the attenuated LOS direction. NLOS-Best directions are critical for maintaining connection when a blockage occurs to the LOS direction and increasing channel rank for multi-stream transmission [15], [25], [26]. NLOS-Best directions usually come from strong reflections from large surfaces of building constructions or furniture. In a word, each LOS TX-RX location pair has one LOS directional PDP, one NLOS-Best directional PDP, and many NLOS directional PDPs. Each NLOS TX-RX location pair has one NLOS-best directional PDP and many NLOS directional PDPs.

Fig. 9 shows the directional path loss scatter plots and best fit CI (1) models for the 142 GHz LOS and NLOS scenarios for the co-polarized (V-V) antenna setup from all four factory sites. Each scatter point denotes a unique pointing direction pair of TX and RX horn antennas with 8° HPBW. For V-V antenna polarizations, the LOS PLE is 2.06, close to the free space PLE of 2, suggesting that the LOS direction only contains a clear optical path within the antenna HPBW without multipath interference. The NLOS PLE was prominently reduced from 5.01 to 3.27 by pointing antennas to the strongest NLOS direction instead of an arbitrary direction, showing the importance of fast and accurate beam steering and alignment in practical communication systems. To have a better characterization of path loss in arbitrary NLOS directions, more path loss measurements should be conducted over distances beyond the range of this measurement campaign (i.e., less

than 5 m and over 85 m). Table III lists the CI path loss model parameters for V-V polarized path loss measurements for separate and lumped datasets of four factory sites. All four factories show LOS PLEs close to free space. However, Site A and Site D produce smaller NLOS and NLOS-Best PLEs than Site B and Site C, possibly because Site A and Site D are more open-planned with fewer partitions and less clutter density.

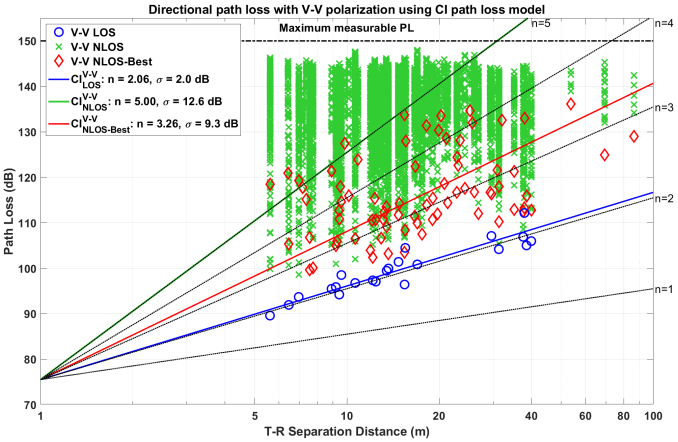

Fig. 9: Directional path loss data and best fit CI path loss models ($d_0 = 1$ m) for V-V polarizations for 142 GHz InF channels from four factory sites.

For the V-H polarized measurements shown in Fig. 10, the LOS, NLOS-Best, and NLOS PLEs are 4.27, 5.16, and 6.17, respectively, which are much greater than the PLEs for V-V antenna polarization due to the polarization mismatch between antennas and channels. The V-H received powers are much weaker than the V-V power and are close to the maximum measurable directional path loss of the channel sounder. In addition, many locations that measured V-V path loss did not have detectable V-H power. Thus, the V-H path loss dataset may have an inherent bias that may lead to a lower PLE than the PLE value using the CI path loss model. However, this limit does not alter the observation that cross-polarized antennas suffer much greater path loss than co-polarized antennas. The CI path loss model produces large PLEs with large variances (σ). Using the PLEs of co-polarized path loss data, the CIX model provides a much better fit than the CI model by reducing the standard deviation from 7.1 dB to 2.9 dB for LOS directions and from 9.4 dB to 6.4 dB for NLOS-Best directions. The XPD for LOS directions is 27.1 dB, close to the antenna XPD measured in free space of 27.5 dB [21]. The NLOS-Best directions produce an XPD of 22.2 dB, and the NLOS directions produce an XPD of 13.3 dB. The NLOS-Best and NLOS directions show an XPD reduction of 5 dB and 14 dB compared to the LOS direction, respectively, indicating that reflection and scattering have a prominent de-polarization effect. The same phenomena were observed in InH environments [15], [25]. Table III lists the CI path loss model parameters for V-H polarized path loss measurements.

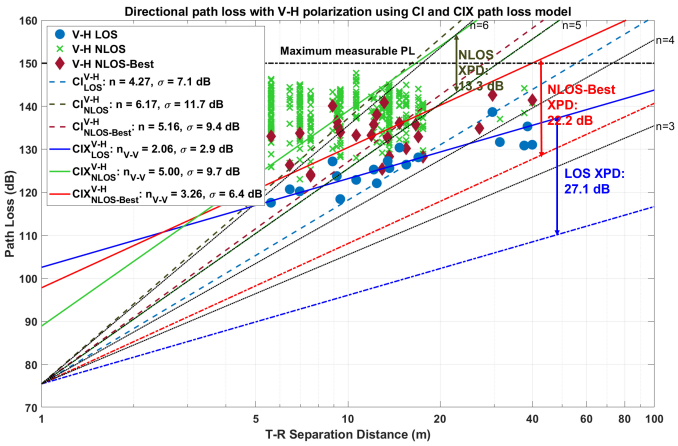

Fig. 10: Directional path loss data and best fit CI and CIX path loss models ($d_0 = 1$ m) for V-H polarization for 142 GHz InF channels from four factory sites.

C. Omnidirectional path loss models for co- and cross-polarized antennas

While the prior directional path loss models match the practical communication systems with antenna arrays forming directional beams, standards organizations such as 3GPP [27] and IEEE [28] need omnidirectional path loss models which allow arbitrary antenna patterns for channel simulations. For each measured pair of TX and RX locations, the omnidirectional received power was recovered by summing the directional received power from every unique TX and RX azimuth and elevation angle combination (with antenna gains subtracted) in linear scale [20]. The omnidirectional received power was then subtracted from the transmitted power to recover the omnidirectional path loss. We consider two scenarios for omnidirectional path loss modeling, LOS and NLOS. The LOS scenario represents the case that there is a clear direct path between the TX and RX with no obstruction. The TX-RX locations with no or partially blocked/attenuated direct path are classified into the NLOS scenario.

Fig. 11 displays the omnidirectional path loss scatter plot and best fit CI and CIX models at 142 GHz in LOS and NLOS environments for co-polarization (V-V) and cross-polarization (V-H) antenna configurations from all four factory sites. Factory sites are denoted as different markers. The V-V and V-H polarized measurements are denoted as empty and filled circles, respectively. For V-V polarization, the LOS PLE is 1.80, which is similar to the value in office environments (1.75) [15] and better than the outdoor environments (1.91) [26]. The NLOS PLE is 3.07, which is worse than 2.7 in office environment [15] and 2.9 in outdoor environment [15], indicating that the factories may be harsh for signal propagation in NLOS scenarios due to 1) dense clutter such as workstations and shelves, 2) large space leading to long propagation distances and a high chance of blockage, 3) smooth surfaces of metallic objects producing only specular reflections with limited scattering. Previous works on channel measurements in factories at mmWave frequencies showed similar PLEs [2], [5], [6], [10]. A summary of CI model parameters for omnidirectional path loss for separate and

TABLE III: Directional CI path loss model (1) parameters with $d_0 = 1$ m for 142 GHz InF channels for V-V and V-H antenna polarization orientations in four factory sites. The TX and RX horn antenna has 27 dBi gain and 8° HPBW. "Pol." stands for TX-RX antenna polarization orientation.

Directional CI Path Loss Models for $d_0 = 1$ m							
Factory	**Pol.**	**LOS**		**NLOS-Best**		**NLOS**	
		PLE	σ (dB)	PLE	σ (dB)	PLE	σ (dB)
A	V-V	2.07	2.3	3.21	9.3	4.48	10.7
	V-H	4.23	7.3	4.96	9.6	5.47	9.1
B	V-V	2.07	1.0	3.58	10.3	5.29	12.6
	V-H	4.72	4.4	4.90	11.2	6.32	12.3
C	V-V	1.95	1.6	3.24	10.3	5.52	13.5
	V-H	3.92	8.7	5.83	3.5	6.26	11.8
D	V-V	2.10	1.8	3.12	7.1	4.92	11.3
	V-H	4.32	5.7	5.41	7.7	6.60	9.1
Total	V-V	2.06	2.0	3.26	9.3	5.00	12.6
	V-H	4.27	7.1	5.16	9.4	6.17	11.7

lumped datasets of four factory sites is given in Table IV.

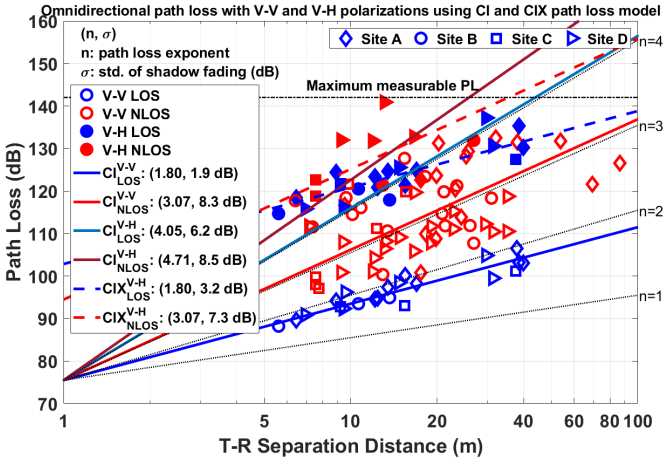

Fig. 11: Omnidirectional CI (1) and CIX path loss models parameters with $d_0 = 1$ m for 142 GHz InF channels for V-V and V-H antenna polarization orientations in four factory sites. Factory sites A–D are denoted as diamond, circle, square, and triangle, respectively. The LOS and NLOS measurements are colored in blue and red, respectively. The V-V and V-H polarized measurements are denoted as empty and filled markers, respectively.

For V-H polarization, the CIX model provides a better fit than the CI model by reducing the standard deviation from 6.2 dB to 3.2 dB for LOS locations and from 7.3 dB to 6.2 dB for NLOS locations. As a result, we observed a more stable XPD across LOS locations than NLOS locations. The omnidirectional LOS and NLOS XPD are 27.3 dB and 19.0 dB, which indicates a significant de-polarization effect in NLOS environments. The CIX model parameters for V-H polarized omnidirectional path loss for separate and lumped datasets for four factory sites are summarized in Table V. We can further confirm that LOS locations present a stable XPD of 27 dB in four factories, while NLOS locations produce a wide range of XPD values in various factories. The difference in the XPD between the LOS and NLOS locations may be because the LOS locations always have a strong boresight optical path which contributes the most received power and does not vary according to the environments. In contrast, the wide range of XPDs at NLOS locations is caused by various environmental layouts and factory building materials.

D. Comparison of path loss between outdoor, office, and factory scenarios

We have conducted extensive propagation measurements at 142 GHz in InH [15], [16], outdoor urban microcell (UMi) [26], [29], and InF [30] scenarios. The directional path loss parameters for LOS, NLOS, and NLOS-Best directions are summarized in Table VI. The LOS PLEs are approximately the same (2.06) across three scenarios, which is close to the free space propagation. The consistency in LOS directional path loss validates that the channel sounding system and data processing methods are reliable and consistent. The PLEs for NLOS-Best directions are 3.26, 3.10, and 3.07 for the InF, InH, and UMi scenarios, respectively. Similarly, the PLEs for the NLOS directions are 5.00, 4.60, and 3.60 for the InF, InH, and UMi scenarios, respectively. Factories show higher PLEs in the NLOS and NLOS-Best directions than the offices and outdoors. A similar trend is observed in the omnidirectional path loss parameters as given in Table VII. The InF and InH scenarios have a similar LOS PLE for omnidirectional path loss, which is better than the UMi scenario. The NLOS PLEs for omnidirectional path loss are 3.07, 2.83, and 2.90 for the InF, InH, and UMi scenarios, respectively. The three scenarios have a similar upper boundary of the 95% confidence interval, but the factories have the highest lower boundary at those NLOS locations. The factories present higher omnidirectional PLE in NLOS than the InH and UMi scenarios may be because of the higher clutter density in the surroundings. The measurements across four factories also show that the resulting PLE is site-specific and varies according to factory size, layout, and clutter. Some previous propagation measurement campaigns conducted in factories at 28 and 33 GHz showed that the PLE obtained from the CI path loss model for the NLOS scenario ranged from 2.7 to 3.3 [4], [8], which agrees with the 142 GHz factory channel measurements introduced above. The expected strong reflections from metallic objects such as workstations and shelves might not always arrive at the RX. Instead, heavy clutter may create additional attenuation or blockage on multipath propagation.

TABLE IV: Omnidirectional CI path loss model (1) parameters with $d_0 = 1$ m for 142 GHz InF channels for V-V and V-H antenna polarization orientations in four factory sites. "Pol." stands for TX-RX antenna polarization orientation.

Factory	Pol.	LOS		NLOS	
		PLE	σ (dB)	PLE	σ (dB)
A	V-V	1.85	1.5	3.19	9.0
	V-H	4.06	6.4	3.78	–
B	V-V	1.72	0.2	3.21	8.8
	V-H	4.26	5.5	4.02	1.1
C	V-V	1.62	1.4	3.33	7.4
	V-H	3.71	8.7	5.15	1.9
D	V-V	1.86	2.2	2.74	5.1
	V-H	4.11	4.0	5.34	5.5
Total	V-V	1.80	1.9	3.07	8.3
	V-H	4.05	6.2	4.71	8.5

TABLE V: Omnidirectional CIX path loss model parameters with $d_0 = 1$ m for 142 GHz InF channels fo V-H antenna polarization orientation in four factory sites. "Pol." stands for TX-RX antenna polarization orientation.

Factory	Pol.	LOS			NLOS		
		PLE ($n_{\text{V-V}}$)	XPD (dB)	σ (dB)	PLE ($n_{\text{V-V}}$)	XPD (dB)	σ (dB)
A	V-H	1.85	27.4	2.5	3.19	7.4	–
B	V-H	1.72	25.5	2.3	3.21	10.4	0.3
C	V-H	1.62	28.5	2.9	3.33	16.0	2.7
D	V-H	1.86	27.4	4.5	2.74	28.8	4.7
Total	V-H	1.80	27.3	3.2	3.07	19.0	7.3

TABLE VI: Comparison of directional path loss parameters between InF, InH, and UMi scenarios.

Directional CI Path Loss Models for $d_0 = 1$ m						
Scenario	**LOS**		**NLOS-Best**		**NLOS**	
	PLE [95% confidence interval]	σ (dB)	PLE [95% confidence interval]	σ (dB)	PLE [95% confidence interval]	σ (dB)
InF [31]	2.06 [1.99, 2.14]	2.0	3.26 [3.07, 3.45]	9.3	5.00 [4.97, 5.03]	12.6
InH [15]	2.05 [1.84, 2.24]	2.9	3.10 [2.68, 3.52]	6.0	4.60 [4.51, 4.69]	13.8
UMi [32]	2.06 [1.93, 2.19]	2.9	3.07 [2.75, 3.39]	8.3	3.60 [3.56, 3.64]	9.1

TABLE VII: Comparison of omnidirectional path loss parameters between InF, InH, and UMi scenarios.

Omnidirectional CI Path Loss Models for $d_0 = 1$ m				
Scenario	**LOS**		**NLOS**	
	PLE [95% confidence interval]	σ (dB)	PLE [95% confidence interval]	σ (dB)
InF [31]	1.80 [1.73, 1.87]	1.9	3.07 [2.87, 3.27]	8.3
InH [15]	1.75 [1.53, 1.97]	3.6	2.83 [2.42, 3.24]	6.1
UMi [32]	1.91 [1.88, 2.04]	2.7	2.90 [2.58, 3.26]	8.2

E. Temporal and Spatial Channel Characteristics for 142 GHz Indoor Factories

Delay spread and angular spread are fundamental indicators of wireless channels. Delay spread represents temporal dispersion and frequency selectivity of the channels, which greatly impacts communication system design. Similarly, angular spread characterizes the angular dispersion of multipath channels. The RMS delay spread σ_τ [33] and the RMS angular spread [27] are the most commonly-used metrics.

Table VIII presents the statistics of RMS omnidirectional delay spread (ODS), RMS directional delay spread (DDS), RMS azimuth angular spread of departure (ASD), and RMS azimuth angular spread of arrival (ASA) for all four factories in the LOS and NLOS scenarios. The statistics include minimum, median, mean, 90% percentile, and maximum values. The azimuth angular spread is calculated based on the measured azimuth angles and the corresponding directional received powers [27]. The directional received power of PDPs captured at the identical azimuth angle but different elevation angles are summed together to represent the total received power in the azimuth angle. Early works on channel measurements in InH and UMi scenarios adopted the same angular spread calculation method [15], [32].

Both ODS and DDS vary across four factories. The mean ODS in the LOS scenario are 20.3 ns, 11.4 ns, 15.9 ns, and 5.5 ns for factory sites A, B, C, and D, respectively. Factories B and D show a larger mean ODS at NLOS locations than LOS locations while factories A and C show a larger mean ODS at LOS locations than NLOS locations. This discrepancy can be attributed to the factory layout and building materials. Factories A and C both have a long center corridor with high obstructions on the sides, which can create strong and long-distance reflections along the corridor and produce a large delay spread. In contrast, factories B and D are large open spaces with machineries, benches, and shelves scattered in the environment, where NLOS locations typically experience more temporal-dispersive channels. Furthermore, the maximum DDS measured in site A and C are 213.4 ns

TABLE VIII: 142 GHz empirical statistics of temporal and angular channel characteristics: omnidirectional delay spread (ODS), directional delay spread (DDS), omnidirectional ASD, omnidirectional ASA for four factory sites in the LOS and NLOS scenarios.

Factory Sites		ODS (ns)		DDS (ns)		ASD (°)		ASA (°)	
		LOS	NLOS	LOS	NLOS	LOS	NLOS	LOS	NLOS
A	Min	0.2	0.0	0.0	0.0	1.7	0.0	0.3	0.0
	Median	9.2	9.1	2.3	0.5	25.7	13.3	32.4	38.6
	Mean	20.3	15.6	17.9	3.0	31.0	18.0	31.6	34.1
	90%	68.2	40.0	59.7	9.0	61.5	42.3	56.6	67.1
	Max	76.6	82.9	213.4	41.6	83.5	68.3	66.2	87.1
B	Min	0.0	1.0	0.0	0.0	3.5	0.8	0.4	9.2
	Median	9.9	13.5	1.4	0.9	32.1	33.7	46.1	31.5
	Mean	11.4	14.9	4.1	4.2	25.4	35.5	44.7	44.4
	90%	24.4	24.4	11.5	15.6	42.6	58.1	75.9	80.6
	Max	24.8	57.9	38.9	49.9	43.3	58.7	76.9	85.6
C	Min	0.6	2.9	0.0	0.0	5.4	11.7	6.0	10.7
	Median	10.6	5.1	2.2	0.2	9.6	17.4	34.2	38.0
	Mean	15.9	5.1	13.4	0.8	23.4	18.8	34.6	37.8
	90%	41.9	7.5	47.8	3.0	69.1	31.0	64.2	58.5
	Max	41.9	7.5	115.1	7.3	69.1	31.0	64.2	58.5
D	Min	0.8	3.0	0.0	0.0	0.7	12.3	3.1	23.1
	Median	6.3	10.8	0.2	0.4	12.9	27.6	21.5	51.3
	Mean	5.5	11.0	1.8	3.2	24.8	29.6	28.4	52.6
	90%	9.9	20.1	5.4	8.5	60.6	57.2	67.8	75.3
	Max	10.3	23.1	18.5	57.0	66.7	61.1	81.2	80.3
All	Min	0.0	0.0	0.0	0.0	0.7	0.0	0.3	0.0
	Median	7.4	9.7	1.4	0.5	23.8	22.5	30.5	40.2
	Mean	14.0	12.8	10.8	3.2	27.2	27.1	33.8	43.7
	90%	39.6	22.1	26.4	8.5	59.4	57.8	66.8	78.2
	Max	76.6	82.9	213.4	57.0	83.5	68.3	81.2	87.1

and 115.1 ns, which are larger than the 38.9 ns and 18.5 ns in site B and D. The median values reveal that 50% of DDS are less than 2.5 ns in all four factory sites, suggesting that communications through highly directional channels require minimal equalization procedure.

The ASD has a smaller mean value than the ASA for both LOS and NLOS scenarios in four factories. For the LOS scenario, the average ASD is 23.8° and the average ASA is 22.5°. For the NLOS scenario, the average ASA is 33.8° and the average ASA is 43.7°. Site B shows the largest median ASD (32.1° and 33.7° for LOS and NLOS) among four factories because site B has the most obstructions such as workstations, machinery, and shelves. Overall, the maximum measured ASD and ASA are 83.5° and 87.1°, indicating that the factory channels have rich multipath scattering because of the heavy clutter. Note that the temporal and spatial distributions of multipaths are essential to understand the factory channel characteristics. A spatial statistical channel model for the InF scenario is left for future development.

F. Comparison of delay/angular spreads between outdoor, office, and factory scenarios

Early propagation measurements have been conducted at 142 GHz in the office [15], [16] and urban [26], [29], [32] scenarios. Table IX summarizes the statistics of 142 GHz channel temporal and angular parameters for three scenarios, InH, UMi, and InF, in LOS and NLOS environments. The temporal parameters are ODS and DDS. The angular parameters are omnidirectional ASD and ASA.

The ODS follows a trend that UMi $>$ InF $>$ InH for both LOS and NLOS environments because the UMi environment has the largest physical dimension. Even though the InF scenario has a maximum ODS (82.9 ns) for the NLOS environment larger than the UMi scenario (56.5 ns), the median value of the InF scenario (12.8 ns) is smaller than the value of the UMi scenario (26.1 ns). All three scenarios produce small median DDS (less than 2 ns) using horn antennas with 8° HPBW at the TX and RX. The 90%-quantile DDS for the InF (8.5 ns for NLOS) and InH (2.6 ns for NLOS) are larger than the values of UMi (0.9 ns for NLOS), suggesting that the indoor environments are more likely to have multiple paths arriving in a similar direction.

The InF scenario has the largest ASD and ASA among the three measured scenarios, which have ASDs of 83.5° and 68.3° for the LOS and NLOS environments and ASAs of 81.2° and 87.1° for the LOS and NLOS environments, respectively. In addition, the InF scenario produces a larger angular spread than the InH and UMi because of the massive existence of metal obstructions (i.e., heavy clutter) in the environments.

IV. Channel Characterization for Antenna Height

According to the terminologies from 3GPP TR 38.901 [27], a device is clutter-elevated if the device antenna is higher than the average environment clutter height. A device is clutter-embedded if the device antenna is lower than the average environment clutter height. A few studies have examined the impact of antenna heights on channel characteristics. Specifically for industrial scenarios, [34] conducted channel measurements at 4.9 GHz in a machine shop (70 m L x 50 m W x 12 m H). The TX and RX were set at 2.5 m (TX)—2.5 m (RX), 2.5 m—1.9 m, 1.9 m—1.9 m, and 1.9 m—0.9 m, respectively. The clutter height ranged from 1.7 m to 3.7 m. The TX is fixed at a corner, and the RX is moved around in the factory. The smallest PLEs are 1.5 and 1.7 for the

TABLE IX: 142 GHz empirical statistics of temporal and angular channel characteristics: omnidirectional delay spread (ODS), directional delay spread (DDS), omnidirectional ASD, omnidirectional ASA for InH [15], UMi [32], and InF in the LOS and NLOS scenarios.

Scenarios		ODS (ns)		DDS (ns)		ASD (°)		ASA (°)	
		LOS	NLOS	LOS	NLOS	LOS	NLOS	LOS	NLOS
InH	Min	0.0	0.0	0.3	0.3	2.5	0.0	8.1	0.0
	Median	3.0	9.3	0.7	0.7	3.7	17.6	35.3	21.1
	Mean	7.2	12.2	3.1	2.2	8.2	28.1	36.0	26.6
	90%	23.0	31.1	10.4	2.6	18.1	79.7	64.1	66.4
	Max	26.4	47.9	52.4	92.5	18.3	80.2	68.4	83.1
UMi	Min	1.5	0.6	0.3	0.3	1.0	0.0	2.9	3.4
	Median	16.3	23.9	0.7	0.6	7.3	3.4	16.8	40.4
	Mean	21.9	26.1	3.0	1.8	8.6	8.7	18.3	39.4
	90%	31.0	47.7	1.1	0.9	20.6	26.3	31.2	63.9
	Max	102.0	56.5	188.7	61.3	21.7	30.7	52.2	66.5
InF	Min	0.0	0.0	0.0	0.0	0.7	0.0	0.3	0.0
	Median	7.4	9.7	1.4	0.5	23.8	22.5	30.5	40.2
	Mean	14.0	12.8	10.8	3.2	27.2	27.1	33.8	43.7
	90%	39.6	22.1	26.4	8.5	59.4	57.8	66.8	78.2
	Max	76.6	82.9	213.4	57.0	83.5	68.3	81.2	87.1

LOS and NLOS environments. The path loss of cross-height setups (i.e., TX and RX at different heights) are higher than the values of co-height setups (i.e., TX and RX at the same height) [34]. [2] conducted 28 GHz channel measurement in a circle-shaped machine hall with a diameter of 63 m and a height of 16 m. The TX was set at 7 m. The RX was set at 1.7 m and 4 m. The 1.7 m RX was embedded by the machines and did not have a LOS path, while the 4.0 m RX was above the machines and always maintained a clear LOS path. The difference in the omnidirectional path loss between high and low RXs has a mean of 3.1 dB with a standard deviation of 2.3 dB. Moreover, the mean RMS ASD for high and low RXs are 37.4° and 41.1°. The mean RMS ASA for high and low RXs are 35.4° and 80.0°. The results show that the ASA has a larger variation than ASD between two antenna heights [2], which agrees with the measurement results explained below.

Here, we conducted comparative propagation measurements at high and low RX heights emulating high (clutter-elevated) user equipment (UE) and low (clutter-embedded) UE at factory site C and D, where the average clutter height is 1 m. The TX was fixed at 2.5 m well above the clutter as an indoor access point. Additional channel measurements with a lower TX height similar to the clutter should be conducted for peer-to-peer communications. Table II summarizes the measurement conducted in factories C and D for the low RX height.

Fig. 12 shows a sample omnidirectional PDP and power angular spectrum (PAS) at TX2 and RX6 in factory site D measured at high and low RX heights. The location of TX2 and RX6 can be found in Fig. 8. A 1-m high machine is between the TX2 and RX6, which does not cause any effect for the high RX, but eliminates the LOS boresight path for the low RX, which is shown as the strongest peak at -40 dBm in Fig. 12a and the lobe at AOD of 270° and AOA of 90° in Fig. 12b. In addition, the low RX receives reflections from the back of the RX from some table legs from AOAs of 210° and 314°. Fig. 12a indicates that the high and low RXs receive some common MPCs at various power levels but may also receive distinct MPCs. The ODS are 3.3 ns and 26.0 ns for the high and low RX, respectively, because of the missing LOS path for the low RX. The omnidirectional RMS ASD are 10.8° and 17.2°, and the omnidirectional RMS ASA are 5.5° and 43.3° for the high and low RX, respectively. The RMS ASD only varies 6.5° while the RMS ASA varies 37.8°, suggesting that ASA has a much larger variation than the ASD. The larger variation of ASA has been observed to be common across various measurement locations.

TABLE X: Channel characteristics including path loss, delay spread, angular spreads for high and low RXs in the LOS and NLOS scenarios.

Channel Characteristics		LOS		NLOS		LOS/NLOS	
		High	Low	High	Low	High	Low
LOS probability		–		–		42%	8%
Omni. PLE (n)		1.82	2.11	2.50	2.88	2.22	2.84
Omni. Path loss (dB)	max	104.8	96.2	111.0	119.6	111.0	119.6
	min	90.8	96.2	100.8	104.2	90.8	96.2
	mean	97.2	96.2	106.2	111.7	102.4	110.4
RMS ODS (ns)	max	10.7	0.7	23.2	16.4	23.2	16.4
	min	1.0	0.7	4.9	3.4	1.0	0.7
	mean	6.8	0.7	12.6	8.9	10.2	8.2
RMS ASD (°)	max	67.6	0.6	62.7	59.9	67.6	59.9
	min	7.2	0.6	8.6	9.2	7.2	0.6
	mean	32.9	0.6	31.1	26.9	31.8	24.7
RMS ASA (°)	max	66.8	16.8	78.3	83.5	78.3	83.5
	min	3.2	16.8	19.1	23.4	3.2	16.8
	mean	28.7	16.8	50.3	52.7	41.3	49.7

A. Impact of Antenna Height on Channel Characteristics

The channel characteristics, including path loss, ODS, and omnidirectional angular spreads for high and low UEs, are summarized in Table X. The maximum, minimum, and mean values are calculated based on the twelve measurement locations in factory site D. The maximum ODS are 23.2 ns and 16.4 ns for the high and low UEs observed in the NLOS scenario. The high UEs have larger mean values of ODS and ASD but a smaller mean value of ASA for the NLOS scenario. In addition, the low UEs have fewer MPCs and time clusters than the high UEs, possibly because the clutter causes more obstructions for the low UEs.

For a clear comparison between the high and low UEs, Table XI provides the statistics of the differences between the high and low UE at each location in channel characteristics such as path loss, ODS, and omnidirectional angular spreads. The maximum, minimum, mean, and standard deviation of the

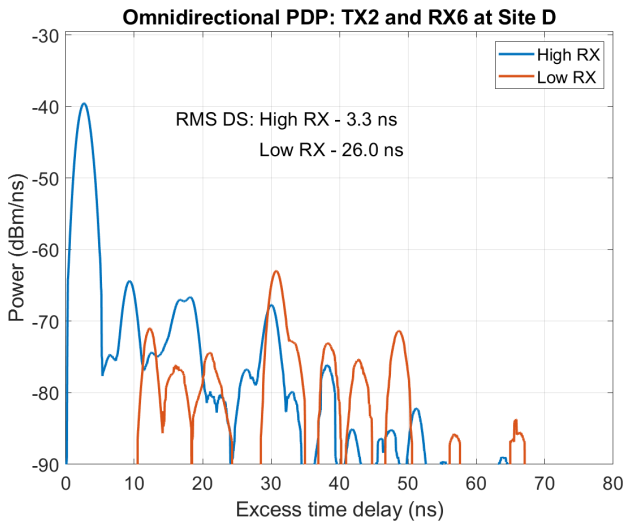

(a) 142 GHz omnidirectional PDP.

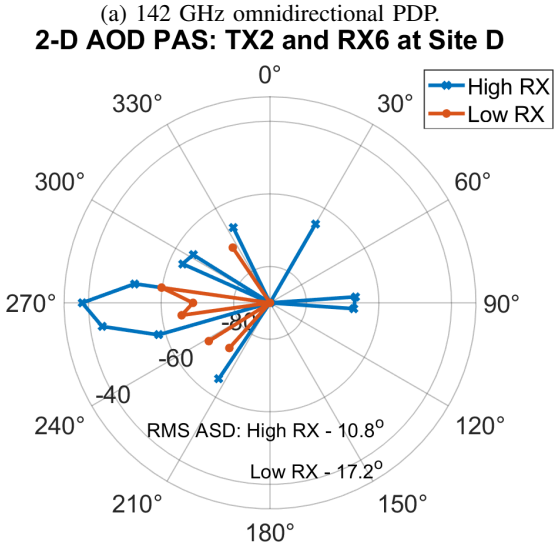

(b) 142 GHz 2-D AOD PAS.

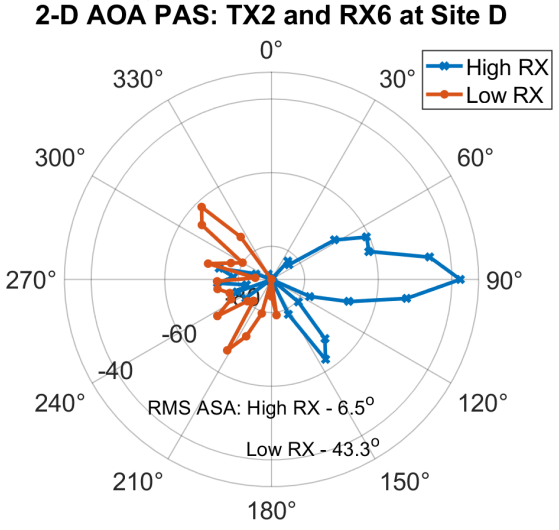

(c) 142 GHz 2-D AOA PAS.

Fig. 12: 142 GHz omnidirectional PDP, 2-D AOD PAS, and 2-D AOA PAS at TX2 and RX6 in factory site D over 7 m TX-RX separation distance. The channel changes from LOS state to NLOS state by decreasing the RX height from 1.5 m to 0.5 m.

TABLE XI: Location-wise variation (Δ) from high to low UEs in channel characteristics. LOS and NLOS represents the LOS visibility of the high RX.

Channel Statistics		LOS Δ	NLOS Δ	LOS/NLOS Δ
Omni. Path loss (dB)	max	-20.8	-13.8	-20.8
	min	-3.8	-1.7	-1.7
	mean	-10.7	-6.0	-8.0
	std	6.3	4.1	5.5
RMS ODS (ns)	max	4.7	19.8	19.8
	min	-15.4	-3.3	-15.4
	mean	-3.8	6.1	3.0
	std	7.2	7.7	8.8
RMS ASD (°)	max	24.6	21.9	24.6
	min	-11.6	-5.2	-11.6
	mean	8.8	5.9	7.1
	std	15.2	9.2	11.5
RMS ASA (°)	max	27.9	46.9	46.9
	min	-60.9	-50.0	-60.9
	mean	-20.4	0.2	-8.4
	std	36.0	31.9	33.8

differences (Δ) are obtained based on the twelve measurement locations in factory site D. The locations are divided into LOS and NLOS locations based on the LOS visibility at high RX. The difference Δ is computed by subtracting the value at a low UE from the value at the corresponding high UE.

As shown in Table XI, the omnidirectional path loss increases at every LOS and NLOS location because the minimum path loss variation is -1.7 dB (i.e., high-UE path loss smaller than low-UE path loss). The maximum path loss increases are 20.8 dB and 13.8 dB in the LOS and NLOS scenarios. The mean path loss increases are 10.7 dB and 6.0 dB in the LOS and NLOS scenarios. The larger path loss increase in the LOS scenario is expected due to the potential blockage of the LOS path. Similarly, the larger standard deviation of 6.3 dB in the LOS scenario also suggests the risk of the diminishing LOS path.

The maximum and minimum ODS variations are 19.8 ns and -15.4 ns, which does not present a monotonous variation from high to low RX heights. The standard deviation of ODS are comparable in the LOS (7.2 ns) and NLOS (7.7 ns) scenarios. The largest ODS decrease of ODS is observed at TX1 with RX4, where the strong reflection from the window at 0° is blocked at the low UE by tables. The largest increase of ODS is observed at TX2 and RX6, where the LOS path is blocked at the low UE by a machine.

The variation of ASD and ASA between the high and low RX heights is highly location-dependent. However, the ASA has a wider variation range than the ASD. In Table XI, the standard deviations of the ASD and ASA variation at LOS locations are 15.2° and 36.0°. The standard deviations of the ASD and ASA variation at NLOS locations are 9.2° and 31.9°. The larger variation of ASA may be attributed to the local clutter surrounding the low UE, which induces more blockages and reflections and prominently changes the angular channel characteristics for low UEs. Similar results were observed in [2], where the mean RMS ASD for high and low RXs are 37.4° and 41.1°. The mean RMS ASA for high and low RXs are 35.4° and 80.0° [2]. In addition, the variation of the number of time clusters and spatial lobes are up to five and three, showing that the channel condition may change prominently

when a clutter-elevated UE becomes a clutter-embedded UE.

V. Channel Enhancement Using Passive Reflecting Surfaces

The 142 GHz InF propagation measurements in Section III show that, in the NLOS scenario, the omnidirectional path loss in factories produces a PLE of 3.1, higher than the InH (PLE=2.7) and the UMi (PLE=2.9). Similar path loss increase is observed at the strongest NLOS directions, producing a directional PLE of 3.2 that is higher than the InH (PLE=3.1) and outdoor UMi (PLE=3.1) environments. In addition, the comparison of channel characteristics between the high and low UEs presented in Section IV suggests that the UEs at a height below surrounding clutter experience additional path loss (omnidirectional PLE increase from 2.5 to 2.9) and prominent channel variation. The measurement results indicate that factories may be a harsh environment for sub-THz communication systems, especially in the NLOS scenario, due to many metallic obstructions such as machinery and workstations. In the industrial environments, manufacturing robotics, automated guided vehicles (AGV), and human workers may enter shadowed areas or cause blockage for other devices, posing challenges to seamless and reliable wireless transmission [30]. Therefore, wireless channels require improvement to counter random blockage, extend coverage, and improve the quality of service for mobile devices connected to industrial wireless networks.

Due to the advent of metamaterials in recent years, reconfigurable intelligent surfaces (RISs) have been proposed to improve wireless network performance by placing one or more low-cost low energy-consuming large metasurfaces in an environment [35]. In particular, RISs might play an important role in factory environments to enable ultra-reliable low-latency communications (URLLC) with massive devices and sensors in the industrial Internet of things (IIOT). RISs can extend the coverage and increase SNR for edge users, form an additional path for increasing spectral efficiency, or set up a transmission link for those devices in outage or blockage to maintain connectivity. There have been only a few prototypes of RISs [36], [37], but these RIS prototypes only have limited configurability and are far from practical deployment. In addition, prototyping of a RIS operating at sub-THz frequencies does not exist, which may require advanced substrate materials such as liquid crystal. Thus, we leverage large and flat metal plates as PRS to gain insights on potential channel improvement using an actual RIS.

Some early work has employed metal surfaces to enhance the propagation channel. A square-shaped metal plate is placed at a fixed position and orientation at the corner of an L-shaped indoor corridor [38]. The measurements study the coverage enhancement down the hallway at 38 GHz and 60 GHz, which achieves a median of 20 dB power gain using a 0.61 m $\times$ 0.61 m and a 0.84 m $\times$ 0.84 m [38]. Li et al. [39] conducted channel measurements at 300 GHz in an indoor corridor. Reflective aluminum foil was attached to the wall next to the entrance to a conference room from the corridor. The foil has a size of 1.2 m $\times$ 1.5 m and does not have a flat surface. The TX is in the corridor, and the RX is in the conference room. An average of 6 dB and 5 dB improvement in the best directional and omnidirectional path loss are achieved [39]. Furthermore, Abbasi et al. [19] conducted outdoor measurements at 140 GHz on a university campus at distances up to 35 m. The pillars were wrapped with aluminum foil and it was observed that the number of MPCs and MPC powers increased due to the aluminum foil. Aluminum foil does not have a flat surface [19], [39], thus cannot provide a clear specular reflection without negligible reflection loss. Moreover, the orientation of the flat metal plate is fixed and cannot emulate the dynamic beamforming of a RIS [38]. Thus, we devise a novel measurement setup using large flat metal plates to improve the propagation channels. The metal plate is fixed on a movable clothing rack and placed near building constructions such as pillars, walls, and corners. The metal plate is rotated manually and carefully in the horizontal plane to find the optimal reflecting orientation, which achieves the strongest reflection power to mimic the RIS beam steering. The channel measurements and modeling for a PRS-aided communication setup are explained as follows.

A. Channel Measurement Procedure with Passive Reflecting Surfaces

We conduct 142 GHz propagation enhancement measurements at factory site D using a 1 m $\times$ 1 m flat metal plate for channel enhancement, as shown in Fig. 8. The TX antenna height is set to 2.5 m above the ground. The RX antenna height is set to 1.5 m and 0.5 m above the ground to study the impact of antenna height and PRS on channel characteristics. Table II summarizes the measurements using PRS for low and high RX in factory D. The PRS measurements are conducted with both RX heights, where most RX locations share the same PRS location at two antenna heights, but a few RX locations use different PRS locations due to the additional obstruction for the low RX. The PRS placement is determined based on the prior channel measurements without any PRS. The PRS location is illustrated as red or blue line segments, following the naming convention of "TX-RX-Height". For example, "1-3H" represents the PRS location for TX1 and high RX3 at 1.5 m height. "2-5L" represents the PRS location for TX2 and low RX5. The center height of the PRS was set to the middle point of the TX and RX antenna heights. Most RXs use the identical PRS location for both high RX and low RX. Some low RXs selected a different PRS location than the corresponding high RXs because the path created by the PRS used for the high RX was blocked for the low RX.

At each measurement location, we follow the measurement procedure described in Section II-C, rotating the TX and RX antennas in the azimuth and elevation planes to record omnidirectional channel responses without a PRS. Then, the PRS position is chosen based on the measured power angular spectrum, from which we can identify an existing single-bounce reflection direction. For LOS locations, the selected reflection direction should not be adjacent to the LOS boresight direction. For NLOS locations, we choose to improve the best reflection direction for those locations with low link margins or to enhance a relatively weak reflection direction for those with existing strong reflections. Such selection principle

This article has been accepted for publication in IEEE Transactions on Wireless Communications. This is the author's version which has not been fully edited and content may change prior to final publication. Citation information: DOI 10.1109/TWC.2023.3337601

can increase the link budget and channel rank for MIMO communications. Finally, a visual ray tracing is performed to identify the reflecting object. Only reflecting objects such as walls, pillars, corners, and large fixed furniture are considered candidate PRS locations because hard or flexible RISs would be installed on large fixed surfaces in future indoor scenarios. The metal plate is then placed next to the reflecting object and is set at a height between the TX and RX, depending on the relative positions. We manually and carefully rotated the metal plate in the horizontal plane to find the best orientation that provided the largest channel gain, which emulates the configurability of RISs steering the beam to the best direction based on channel estimation. With the TX antenna fixed, the RX antenna is swept over 360° in the azimuth plane in step increments of the antenna HPBW of 8°. Identical azimuth sweeps are performed at three elevation planes, which are boresight, 8° above and below the boresight. The adjacent azimuth TX pointing directions with 8° spacing that show sufficient reflecting power are measured at several locations.

Prior channel measurements without PRS show first-order (i.e., single-bounce) reflections have a major contribution to the total received power. Furthermore, because the PRS is set to enhance an existing first-order reflection path, other TX pointing directions that do not point to the metal plate are not measured with PRS. Even though other TX pointing angles may also be influenced (enhanced or attenuated) by the placed metal plate, the power variation and the effect on the omnidirectional channel are expected to be minimal because these paths propagate through multiple reflections.

B. Channel Characterization with Passive Reflecting Surfaces

The 142 GHz channel measurements record directional PDP using narrowbeam horn antennas of 8° HPBW at the TX and RX. Sample omnidirectional PDP and PAS are shown in Fig. 13. For TX1 and RX4H, the PRS is placed at the pillar as illustrated in Fig. 8, the TX is pointed at 18°, and the RX is swept in the azimuth plane. The omnidirectional PDP in Fig. 13a shows that the power of three MPCs were increased by the PRS. It can be seen from Fig. 13b that the first MPC was the first-order reflection from the pillar and the second MPC is reflected from the wall on the south of RX4. For TX3 and RX7, the second strongest MPC becomes the strongest one after placing the PRS, which increases the path power from -67 dBm to -46 dBm providing a 19 dB gain. Fig. 13b shows that two AOA directions are influenced by the PRS. We observed that the PRS could provide strong specular reflection, where the AOAs from the front and back reflection show increased received power.

The directional path loss reduction in the reflecting direction enhanced by the PRS is shown in Fig. 14a location by location, where, for each TX-RX location pair, the TX-RX antenna pointing combination that presents the maximum directional power gain is plotted. Note that the directional path loss power is calculated by summing all the samples recorded in a directional PDP, which may contain multiple MPCs. The PRS provides a mean power increase of 25 dB with a maximum of 37.8 dB and a minimum of 6.6 dB. The TX2 and low RX6 show the maximum gain of 37.8 dB because

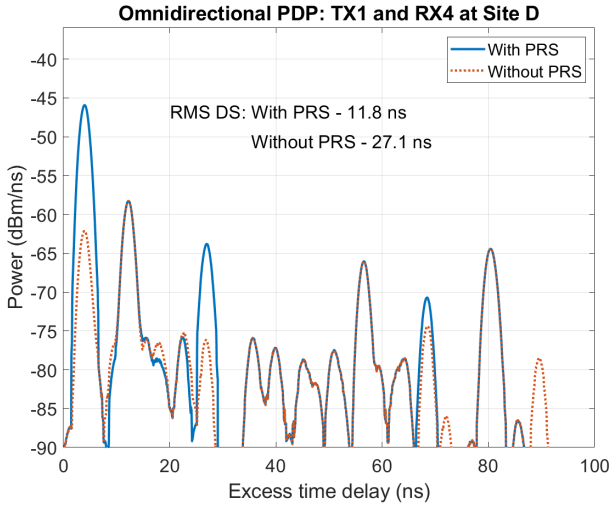

(a) 142 GHz omnidirectional PDP with and without a PRS.

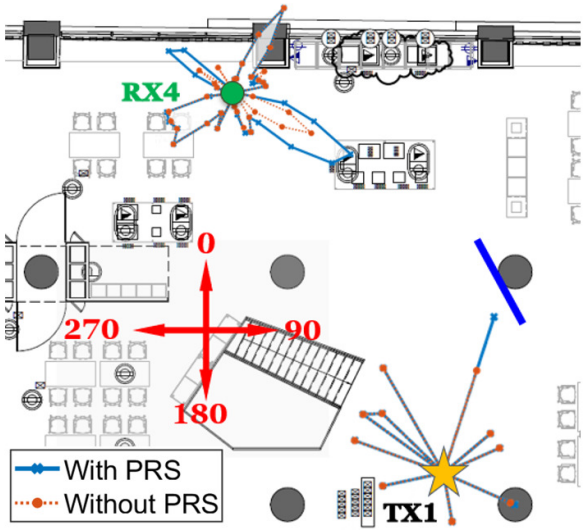

(b) 142 GHz AOD and AOA PAS with and without a PRS.

Fig. 13: 142 GHz omnidirectional PDP, 2-D AOD PAS, and 2-D AOA PAS at TX1 and RX4 in the NLOS scenario in factory site D over 12 m TX-RX separation distance. The PRS is illustrated as a short blue line segment.

the distance between the TX2, PRS2-6L, and RX6 is the shortest among all the measurement locations. In addition, the reflection from the partition wall where PRS2-6L is located is partially blocked by the machinery near the RX6 without the aid of a PRS. In contrast, the PRS2-6L emulates an anomalous reflector that does not obey the specular reflection from the original furniture surface and creates a strong single-bounce reflection path. The statistics of directional path loss difference in the PRS reflecting direction are provided in Table XII. The LOS and NLOS locations show a similar mean and standard deviation of directional path loss, indicating that the reflecting direction enhanced by PRS does not interfere with the boresight path.

The TX2 and low RX8 present the minimum directional path power gain of 6.6 dB because the signal is transmitted over the largest TX-RX separation distance of 38 m measured in site D, where many machines and tables are located between

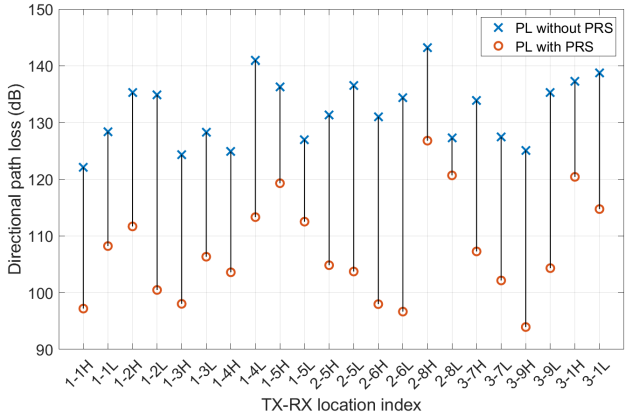

(a) Directional path loss reduction with PRS aid.

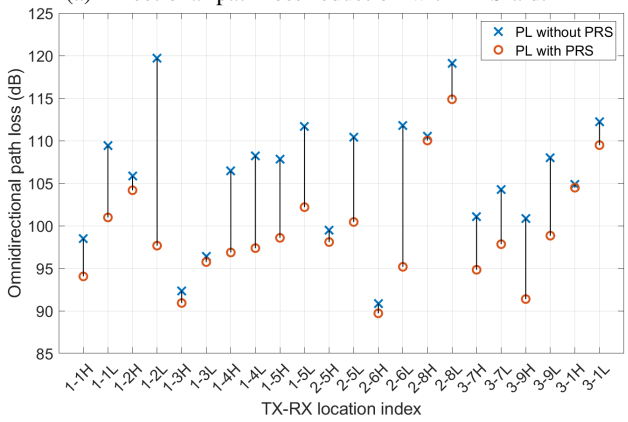

(b) Omnidirectional path loss reduction with PRS aid.

Fig. 14: Directional and omnidirectional path loss comparison between the natural channels and the PRS-aided channels.

TABLE XII: Channel characteristics and the difference (Δ) between the no-PRS and with-PRS channels.

Channel Statistics		No PRS		With PRS		Δ	
		LOS	NLOS	LOS	NLOS	LOS	NLOS
Omni. PLE		1.86	2.73	1.73	2.08	0.13	0.65
Dir. PLE		—	4.55	—	2.60	—	1.95
Omni. PL (dB)	min	90.9	100.9	89.7	91.4	0.4	0.5
	max	104.9	119.7	104.5	114.9	4.4	22.0
	mean	97.1	109.2	95.5	100.7	1.6	8.5
	std	5.1	5.3	5.4	6.2	1.5	5.4
Dir. best PL (dB)	min	122.1	124.9	97.2	93.9	16.8	6.6
	max	137.2	143.2	120.4	126.8	33.0	37.8
	mean	129.1	133.1	104.1	108.7	24.9	24.4
	std	5.4	5.7	8.9	9.0	5.4	8.2
Omni. DS (ns)	min	1.6	2.7	5.8	1.6	-7.9	-7.5
	max	12.2	27.1	14.8	17.1	3.2	20.3
	mean	6.8	10.1	9.9	6.2	-3.1	3.9
	std	4.0	7.1	3.6	4.6	4.3	6.7
Omni. ASA (°)	min	6.5	18.0	21.3	11.6	-35.4	-38.2
	max	63.0	87.9	72.5	73.2	19.9	57.4
	mean	32.6	51.3	38.0	33.0	-5.4	18.3
	std	19.0	23.6	19.6	19.1	18.6	24.9

the TX and RX causing partial blockage. Thus, the link created by the PRS does not have a clear first-order reflection path, indicating that the choice of location of PRS2-8L might not be optimal. Instead, a location in the proximity of the RX may present a better enhancement performance. RIS placement strategy is also an important research topic to provide optimal coverage and enhancement, requiring a minimal number of RISs. A PRS can significantly reduce the directional PLE from 4.55 to 2.60 in the enhanced direction.

Fig. 14b shows the influence of the PRS on omnidirectional path loss. The PRS increases the directional power by a maximum of 22 dB and a minimum of 0.5 dB with a mean of 6.5 dB. This increase depends on the PRS and other existing MPCs. A small increase indicates that other MPCs are dominating the total received power, which is a common case for the LOS scenario. However, a significant increase often occurs at NLOS and near-outage locations, where the PRS-enhanced path becomes the strongest path and dominates the channel.

Placing a PRS in the environment does not necessarily increase or decrease the delay spread at every location. The average ODS increases from 6.8 ns without the PRS to 9.9 ns with the PRS at LOS locations while the average ODS reduces from 10.1 ns to 6.2 ns at NLOS locations. The maximum increase and decrease of the ODS are 20.3 ns and 7.9 ns, respectively. The measured ASA ranges from 11.6° to 73.2°, which also does not present a universal increase or decrease. The maximum increase and decrease of the omnidirectional ASA are 57.4° and 38.2°. Thus, channel estimation and real-time system reconfiguration at base stations and mobile devices are crucial for optimal RIS-aided communication performance. Table XII summarizes the statistics of the channel properties and the difference (Δ) between the channel with and without PRS over all measurement locations as shown in Fig. 14.

VI. Conclusions

This work explores the sub-THz communications in industrial scenarios for smart factories that are envisioned to support Tbps networks and centimeter-level sensing/positioning in 6G and beyond. The omnidirectional path loss measurements yield PLE of 1.8 and 3.1 for the industrial LOS and NLOS scenarios at 142 GHz, respectively. The NLOS PLE of factories is higher than the values in offices (PLE=2.8) and urban scenarios (PLE=2.9), suggesting that the factories can be harsh for sub-THz signals, especially in the NLOS environments, due to the heavy clutter such as machinery, workstations, and tall shelves. Furthermore, the propagation measurements with a near-the-ground RX show that near-the-ground UEs such as AGVs often experience larger path loss (i.e., 10.7 dB and 6.0 dB increase on average over all LOS and NLOS locations) compared to a high RX due to a higher probability of blockage and scattering loss caused by surrounding obstructions. The ASA difference of 33.8° between the low and high RXs is larger than the ASD variation of 11.5°, suggesting that local clutter surrounding the low RX changes the channel condition significantly. In addition, the channel enhancement measurements demonstrate that a single large metal plate

(i.e., PRS) can provide an average gain of 25 dB in the desired pointing directions by accurately orientating the plate. In general, the PRS increases the omnidirectional received power by a maximum of 22 dB and a minimum of 0.5 dB with a mean of 6.5 dB, thus providing better coverage, which suggests that future implementations and deployments of RISs and PRSs can play an essential part in sub-THz wireless systems. This work provides insights on factory channel model standardization above 100 GHz and may motivate more effort on sub-THz channel measurement and wireless system designs for future smart factories in 6G and beyond.

REFERENCES

[1] T. S. Rappaport, Y. Xing, O. Kanhere, S. Ju, A. Madanayake, S. Mandal, A. Alkhateeb, and G. C. Trichopoulos, "Wireless communications and applications above 100 GHz: Opportunities and challenges for 6G and beyond," *IEEE Access*, vol. 7, pp. 78 729–78 757, 2019.

[2] M. Schmieder, F. Undi, M. Peter, E. Koenig, and W. Keusgen, "Directional wideband channel measurements at 28 GHz in an industrial environment," in *2019 IEEE Global Communications Conference (GLOBECOM)*, 2019, pp. 1–6.

[3] M. Schmieder, T. Eichler, S. Wittig, M. Peter, and W. Keusgen, "Measurement and characterization of an indoor industrial environment at 3.7 and 28 GHz," in *2020 14th European Conference on Antennas and Propagation (EuCAP)*, 2020, pp. 1–5.

[4] D. Solomitckii, M. Allén, D. Yolchyan, H. Hovsepyan, M. Valkama, and Y. Koucheryavy, "Millimeter-wave channel measurements at 28 GHz in digital fabrication facilities," in *2019 16th International Symposium on Wireless Communication Systems (ISWCS)*, 2019, pp. 548–552.

[5] D. Chizhik, J. Du, R. A. Valenzuela, J. Otterbach, R. Fuchs, and J. Koppenborg, "Path loss and directional gain measurements at 28 GHz for factory automation," in *2019 IEEE International Symposium on Antennas and Propagation and USNC-URSI Radio Science Meeting*, 2019, pp. 2143–2144.

[6] S. Ito, T. Hayashi, K. Yamazaki, M. Nakao, S. Sakai, Y. Kurosawa, A. Matsunaga, and K. Yoshida, "Measurement and modeling of propagation characteristics for an indoor environment in the 28 GHz-band," in *2019 IEEE 30th Annual International Symposium on Personal, Indoor and Mobile Radio Communications (PIMRC)*, 2019, pp. 1–6.

[7] Y. Wang *et al.*, "Measurement-based analysis and modeling of channel characteristics in an industrial scenario at 28 GHz," in *2021 IEEE 94th Vehicular Technology Conference (VTC2021-Fall)*, 2021, pp. 1–5.

[8] D. Dupleich, R. Müller, M. Landmann, J. Luo, G. D. Galdo, and R. S. Thomä, "Multi-band characterization of propagation in industry scenarios," in *2020 14th European Conference on Antennas and Propagation (EuCAP)*, 2020, pp. 1–5.

[9] D. Dupleich, N. Han, A. Ebert, R. Muller, S. Ludwig, A. Artemenko, J. Eichinger, T. Geiss, G. Del Galdo, and R. Thomä, "From sub-6 GHz to mm-wave: Simultaneous multi-band characterization of propagation from measurements in industry scenarios," in *2022 16th European Conference on Antennas and Propagation (EuCAP)*, 2022, pp. 1–5.

[10] A. Al-Saman, M. Mohamed, M. Cheffena, and A. Moldsvor, "Wideband channel characterization for 6G networks in industrial environments," *Sensors*, vol. 21, no. 6, 2021.

[11] T. S. Rappaport, "Characterization of UHF multipath radio channels in factory buildings," *IEEE Transactions on Antennas and Propagation*, vol. 37, no. 8, pp. 1058–1069, Aug 1989.

[12] C. Cano, G. H. Sim, A. Asadi, and X. Vilajosana, "A channel measurement campaign for mmWave communication in industrial settings," *IEEE Transactions on Wireless Communications*, vol. 20, no. 1, pp. 299–315, 2021.

[13] Y. Xing and T. S. Rappaport, "Propagation measurement system and approach at 140 GHz-moving to 6G and above 100 GHz," in *2018 IEEE Global Communications Conference (GLOBECOM)*, 2018, pp. 1–6.

[14] G. R. MacCartney and T. S. Rappaport, "A flexible millimeter-wave channel sounder with absolute timing," *IEEE Journal on Selected Areas in Communications*, vol. 35, no. 6, pp. 1402–1418, 2017.

[15] S. Ju, Y. Xing, O. Kanhere, and T. S. Rappaport, "Millimeter wave and sub-Terahertz spatial statistical channel model for an indoor office building," *IEEE Journal on Selected Areas in Communications*, vol. 39, no. 6, pp. 1561–1575, 2021.

[16] Y. Xing, T. S. Rappaport, and A. Ghosh, "Millimeter wave and sub-THz indoor radio propagation channel measurements, models, and comparisons in an office environment," *IEEE Communications Letters*, vol. 25, no. 10, pp. 3151–3155, 2021.

[17] Y. Chen, Y. Li, C. Han, Z. Yu, and G. Wang, "Channel measurement and ray-tracing-statistical hybrid modeling for low-Terahertz indoor communications," *IEEE Transactions on Wireless Communications*, vol. 20, no. 12, pp. 8163–8176, 2021.

[18] Y. Li, Y. Wang, Y. Chen, Z. Yu, and C. Han, "Channel measurement and analysis in an indoor corridor scenario at 300 GHz," in *ICC 2022 - 2022 IEEE International Conference on Communications (ICC)*, 2022, pp. 1–6.

[19] N. A. Abbasi, J. Gomez-Ponce, S. M. Shaikbepari, S. Rao, R. Kondaveti, S. Abu-Surra, G. Xu, C. Zhang, and A. F. Molisch, "Ultra-wideband double directional channel measurements for THz communications in urban environments," in *ICC 2021 - IEEE International Conference on Communications*, 2021, pp. 1–6.

[20] S. Sun, G. R. MacCartney, M. K. Samimi, and T. S. Rappaport, "Synthesizing omnidirectional antenna patterns, received power and path loss from directional antennas for 5G millimeter-wave communications," in *2015 IEEE Global Communications Conference (GLOBECOM)*, 2015, pp. 1–7.

[21] D. Shakya, T. Wu, M. E. Knox, and T. S. Rappaport, "A wideband sliding correlation channel sounder in 65 nm CMOS: Evaluation board performance," *IEEE Transactions on Circuits and Systems II: Express Briefs*, vol. 68, no. 9, pp. 3043–3047, 2021.

[22] S. Sun, T. S. Rappaport, T. A. Thomas, A. Ghosh, H. C. Nguyen, I. Z. Kovács, I. Rodriguez, O. Koymen, and A. Partyka, "Investigation of prediction accuracy, sensitivity, and parameter stability of large-scale propagation path loss models for 5G wireless communications," *IEEE Transactions on Vehicular Technology*, vol. 65, no. 5, pp. 2843–2860, 2016.

[23] T. S. Rappaport *et al.*, "Millimeter wave mobile communications for 5G cellular: It will work!" *IEEE Access*, vol. 1, pp. 335–349, May 2013.

[24] T. S. Rappaport, G. R. MacCartney, M. K. Samimi, and S. Sun, "Wideband millimeter-wave propagation measurements and channel models for future wireless communication system design," *IEEE Transactions on Communications*, vol. 63, no. 9, pp. 3029–3056, 2015.

[25] G. R. Maccartney, T. S. Rappaport, S. Sun, and S. Deng, "Indoor office wideband millimeter-wave propagation measurements and channel models at 28 and 73 GHz for ultra-dense 5G wireless networks," *IEEE Access*, vol. 3, pp. 2388–2424, 2015.

[26] Y. Xing and T. S. Rappaport, "Propagation measurements and path loss models for sub-THz in urban microcells," in *ICC 2021 - IEEE International Conference on Communications*, 2021, pp. 1–6.

[27] 3GPP, "Technical specification group radio access network; study on channel model for frequencies from 0.5 to 100 GHz (Release 16)," TR 38.901 V16.0.0, October 2019.

[28] A. Maltsev *et al.*, "Channel models for 60 GHz WLAN systems," doc.: IEEE 802.11-09/0334r8, May 2010.

[29] S. Ju and T. S. Rappaport, "Sub-Terahertz spatial statistical MIMO channel model for urban microcells at 142 GHz," in *2021 IEEE Global Communications Conference (GLOBECOM)*, 2021, pp. 1–6.

[30] S. Ju, Y. Xing, O. Kanhere, and T. S. Rappaport, "Sub-Terahertz channel measurements and characterization in a factory building," in *2022 IEEE International Conference on Communications (ICC)*, May 2022, pp. 1–6.

[31] S. Ju and T. S. Rappaport, "142 GHz multipath propagation measurements and path loss channel modeling in factory buildings," in *ICC 2023 - IEEE International Conference on Communications*, 2023, pp. 1–6.

[32] Y. Xing and T. S. Rappaport, "Millimeter wave and Terahertz urban microcell propagation measurements and models," *IEEE Communications Letters*, vol. 25, no. 12, pp. 3755–3759, 2021.

[33] T. S. Rappaport, *Wireless Communications: Principles and Practice*, 2nd ed. Upper Saddle River, NJ: Prentice Hall, 2002.

[34] T. Jiang, L. Tian, J. Zhang, Y. Zheng, Q. Wang, and J. Dou, "The impact of antenna height on the channel model in indoor industrial scenario," in *2020 IEEE/CIC International Conference on Communications in China (ICCC Workshops)*, 2020, pp. 1–6.

[35] X. Ni, A. V. Kildishev, and V. M. Shalaev, "Metasurface holograms for visible light," *Nature Communications*, vol. 4, no. 1, p. 2807, Nov. 2013.

[36] X. Pei, H. Yin, L. Tan, L. Cao, Z. Li, K. Wang, K. Zhang, and E. Björnson, "RIS-aided wireless communications: Prototyping, adaptive beamforming, and indoor/outdoor field trials," *IEEE Transactions on Communications*, vol. 69, no. 12, pp. 8627–8640, 2021.

[37] W. Tang, M. Z. Chen, X. Chen, J. Y. Dai, Y. Han, M. Di Renzo, Y. Zeng, S. Jin, Q. Cheng, and T. J. Cui, "Wireless communications with reconfigurable intelligent surface: Path loss modeling and experimental

measurement," *IEEE Transactions on Wireless Communications*, vol. 20, no. 1, pp. 421–439, 2021.

[38] W. Khawaja, O. Ozdemir, Y. Yapici, F. Erden, and I. Guvenc, "Coverage enhancement for nlos mmWave links using passive reflectors," *IEEE Open Journal of the Communications Society*, vol. 1, pp. 263–281, 2020.

[39] Y. Li, Y. Wang, Y. Chen, Z. Yu, and C. Han, "Channel measurement and coverage analysis for NIRS-aided THz communications in indoor environments," arXiv:2303.08327 [cs], Jun. 2023.